Article

Plasmonic Metasurfaces for Superposition of Profile-Tunable Tightly Focused Vector Beams and Generation of the Structured Light

**Lianmeng Li [1], Xiangyu Zeng [1], Manna Gu [1], Yuqin Zhang [1,2], Rui Sun [1], Ziheng Zhang [1], Guosen Cui [1], Yuxiang Zhou [1], Chuanfu Cheng [1,* and Chunxiang Liu [1,*

[1] College of Physics and Electronics, Shandong Normal University, Jinan 250014, China
[2] School of Science, Shandong Jianzhu University, Jinan 250101, China
* Correspondence: chengchuanfu@sdnu.edu.cn (C.C.); liuchunxiang@sdnu.edu.cn (C.L.)

Abstract: Vector beams (VBs) and their superposition have found important applications in versatile fields such as optical communications, super-resolution microscopy and quantum information, and metasurfaces have enabled the miniaturization and integration of the optical systems manipulating the vector beams, providing potential applications to subwavelength regimes. In this work, we propose a metasurface to realize the superposition of profile-tunable tightly focused VBs, with the novel structured light fields generated. The metasurface is composed of two sets of orthogonal-nanoslit pairs arranged on the inner and outer rings. By realizing the chiral conversion of circularly polarized light with the slit-pairs which act as half-wave plates, and by creating helical phase profiles of optical vortices with the geometrical phase of rotational nano-slit pairs, two focused Bessel VBs are formed. By finely varying the diameters of two sets of rings, the doughnuts of the two Bessel VBs of different orders are tuned to be of the same size, and the superposition of the two VBs is realized. The theoretical analyses of the superimposed fields were presented, the FDTD simulations were performed to optimize the designed metasurfaces, and the experimental measurements were carried out to validate feasibility of the metasurface. The novel and interesting characteristics of the superposed fields different from those of the conventional VBs were demonstrated. This work will be of significance for classical and quantum applications of VBs in various fields.

Keywords: metasurface; vector beams; geometrical phase; orthogonal-nanoslit pairs

1. Introduction

Metasurfaces are an artificial anisotropic surface structure consisting of sub-wavelength periodic units [1–3]. With the interaction of light with the structural units, metasurfaces can be used to flexibly control the properties of the output wavefields including the phases, amplitudes, and polarizations, exhibiting the powerful capabilities to manipulate the electromagnetic field wavefront. Compared with conventional bulky devices, metasurfaces have the advantages of high resolution, miniaturization, and feasibility for fabrications, and have found important applications in a wide range of areas such as metalenses [4–6], optical holography [7–10], medical detection [11–14] and structural color [15–18]. In manipulation of light fields with the metasurfaces, one of the most fundamental methods is to use the wavelength-dependent resonance of the metasurface units functioning as waveplates, with a propagation phase from 0 to 2π imparted by changing the size and shape of the units [19–22]. Another important and more widely used method is to employ the geometric phase shift $2\sigma\theta$ that depends on the circular polarizations of the chirality σ and the change of orientation angle θ of the units. Greatly facilitating the phase and polarization control, this method has realized the comprehensive manipulations of the light field at nano-scale, and it has brought about rapid advances in the engineering and applications of metasurfaces in recent years. Up to now, geometric phase has been used to design the

metasurfaces with different functionalities for versatile applications. To mention a few examples in the vast amount of literature, L. L. Huang et al. proposed a metasurface of nanorods with variant orientations [23] and investigated phase discontinuity and the vortex generation via the conversion of circular polarization chirality; M.A. Zaman et al. [24], W.Y. Tsai et al. [25] and Y. Zhang et al. [26] proposed plasmonic spiral metasurfaces to realize the selective trapping or rotation of microparticles and the generation of vector vortex beams. M. Kim et al. [27] and W. J. Luo et al. [28] proposed dielectric and plasmonic metasurfaces to realize the photonic spin Hall effect of high efficiency for the circular polarization separations. Recently, by using the geometrical phase synthesized with the propagation phase, the deflection of optical vortices to independent directions was performed in the quadruplex circular polarization channels [29]; with the multiplexed meta-atoms, the quasi-perfect vortices of independent topological charges were generated [30]. Particularly, the geometric phase supports the spin-orbit angular momentum conversion of the metasurfaces, enabling them to possess conspicuous capabilities to manipulate the structured light field such as optical vortex, vector beams and their superposition.

Vector beams (VBs) are light fields with a spatially inhomogeneous distribution of polarizations; they are essentially the superposition of orbital angular momentum (OAM) modes carrying the spin angular momentum (SAM), and they are categorized into the most important types of structured light [31,32]. Over the past decade, they have attracted significant research interest and have found applications in a wide range of fields from classical physics to quantum science. The typical classical applications of VBs include high-resolution microscopy [33], light particle trapping [34,35], and medical clinical detection [36]. Fundamentally, the inseparability of the SAM and OAM modes of a VB is similar to the local entanglement in a bipartite quantum system; and VBs are used as a novel resource for quantum information protocols to encode rotationally invariant qubits [37–39] and have applications to quantum walk [40] and teletransportation [41], quantum error correction [42], quantum state tomography [43], etc. As the prior work, the generation of VBs have received great attention, and a series of methods and devices have been developed, such as q-plates [44], spatial light modulators [38,45], intracavity mode devices [46] and fiber lasers with mode-selective coupler [47]. It is a familiar characteristic of the VBs that the doughnut size in the intensity profiles is enlarged with the increase of the topological charges. This property is similar to that of vortex beams, and it was encountered earlier in the OAM-mode division multiplexing for enhanced data transmission in optical fiber communications [48,49], while the doughnuts of different sizes caused difficulties to couple multiple OAM beams of different topological charges into a fiber with an annular refractive index profile. The perfect optical vortices (POVs) were proposed [50,51] to overcome the difficulty, and such beams had the doughnut radius independent of the topological charges. Up to present, versatile schemes have been developed to generate POVs, making them suitable for propagations in the fiber [52,53] and for other applications. Moreover, the perfect VBs (PVBs) [54] were also proposed and garnered great interest [55–57] owing to their potential in extensive fields. Yet, the bulky optical paths to engender the PVBs with the conventional optical components make miniaturized integration impractical.

The generation of nanoscale VBs with metasurfaces has achieved rapid advancements, and various metasurfaces have been engineered to generate different VBs, including the simple radial and azimuthal polarized VBs (RPVBs and APVBs) and the higher-order Poincaré (HOP) VBs in single- and multi-channels [58–62]. Particularly, the PVBs [57,63] have been generated by introducing an axicon in either geometric or propagation phase in the metasurfaces, and they have found important applications in ultra-secure optical encryption [64], high-capacity optical communications [65,66] and particle capture [35,67]. Nevertheless, the additional phase of axicon produced the symmetrical deflection in focusing the wavefronts, and it has led to a diameter of the doughnut of the PVBs (usually on the scale of tens of micrometers) much larger than the tightly focused VBs; this weakened the ability of the PVBs for strong trapping and manipulations of particles. On the other hand, as an interesting discovery, tightly focused beams have supported a

series of important phenomena such as spin-orbit interactions [68], topological structures in light field [69] and super-resolution [70,71]. However, in generating the tightly-focused VBs with metasurfaces, the doughnuts of intensity profiles for the generated beams are usually dependent on the topological charges, and how to tune the doughnut sizes so as to make them independent of the topological charges still needs to be tackled. Furthermore, through the superpositions of the circularly polarized vortices, generations of the ordinary VBs and the PVBs are widely studied. However, the superposition of tightly focused VBs with tunable intensity profiles has been rarely investigated.

In this paper, by spatially multiplexing the orthogonal nano-slit pairs arranged on circular rings, we design a metasurface to realize the superposition of profile-tunable tightly focused VBs and to generate the involved structured light. The metasurface is composed of the nano-slit pairs arranged on two sets of rings; each set includes both the inner and outer rings with different radii, and they have an optical path difference of a half wavelength to the center point of the observation plane. With combination of the path difference and the orthogonality of the two slits, each slit-pair acts as a half-wave plate and realizes the chiral conversion of incident circularly polarized light; meanwhile, the circularly polarized vortex beams with helical profiles based on the rotation of each nano-slit pairs are produced, and two Bessel VBs are formed under illumination of linearly polarized light. The two VBs are generated by the diffraction of wavefronts from the two sets of slit-pairs on corresponding rings. The larger diameter of the ring with respect to the observation distance provides a larger equivalent numerical aperture, causing the two Bessel VBs to be tightly focused. By precisely changing the diameters of two sets of rings, the doughnuts of the two Bessel VBs of different orders are tuned to be of the same size, thus realizing the superposition of two profile-tunable tightly focused VBs. To perform the metasurface design and demonstrate the superposition of the VBs, we gave the theoretical analysis of the superimposed fields produced by the metasurface; then we performed the simulations using the finite difference in time domain (FDTD) to optimize the designed metasurfaces; finally, we fabricated metasurface samples and carried out experimental measurements. This work would be of significance for applications of metasurfaces and VBs in high-capacity optical communication, optical information encryption and particle manipulations.

2. Basic Principles

Figure 1 is the illustrative schematic for the design principle of the metasurface to realize the superposition of tightly focused VBs of tunable profile, and the metasurface is composed of spatially multiplexed orthogonal slit-pairs. Figure 1a illustrates the wavefront propagation of the superimposed light field. Two sets of orthogonal nano-slit pairs interleaved in the metasurface are etched in an Au film deposited on a SiO_2 substrate; they are specified as the inner and outer sets of slit-pairs according to the radii of the rings, whereas the slits have the same size and the orientation angles of the slit-pairs rotate with the azimuths. For clarity and convenience, the slits in each set of slit-pairs are also signified as inner-ring slits and outer-ring slits, respectively. Under the illumination of linearly polarized light, a set of slit-pairs produces both the left-handed and right-handed circularly polarized vortices $|L, -q>$ of order $-q$ and $|R, q>$ of order q, yielding the VB of order q; while for both the inner and outer sets of slit-pairs, the tightly focused VBs of orders $q = n$ and $q = g$ are produced at the same time, respectively, and the superposition of the two VBs are realized. Since the light field of each VB in the area near the center point O' of the observation plane are simply the Fourier transform of the waves from the corresponding set of slit-pairs, the doughnut size of intensity profile is decreased with the increase of the corresponding slit-pair ring. Thus, by controlling the rotational orders of the two sets of slit-pairs and adjusting the radii of the two sets of slit-pair rings, the doughnuts of the VBs of the orders n and g can be tuned to be with the same size, and the superposition of the two VBs with equal doughnuts is realized.
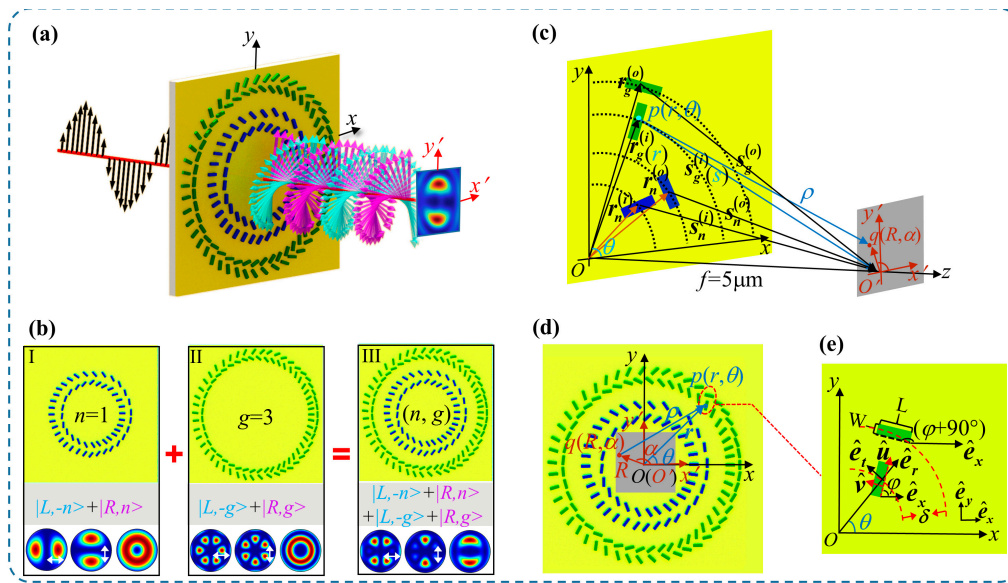
Figure 1. (**a**) Schematic for superposing the profile-tunable tightly focused VBs by metasurface. (**b**) The principle illustration for the metasurface superposes the VBs of the orders $n = 1$ and $g = 3$ with equal light intensity profiles. Panel I: metasurface of inner set slit-pairs; Panel II: metasurface of outer set slit-pairs; Panel III: metasurface consists of inner and outer sets slit-pairs. The white double arrows show the transmitting direction of the analyzing polarizer. (**c**) Geometry and coordinate relations for points on the object and observations planes. The two sets of the orthogonal slit-pairs and the rings the slits lie on are illustrated. (**d**) The overlapping view of the object plane *Oxy* and the observation plane *O′x′y′*. (**e**) Schematic for unit vectors of the coordinates and orientations of slits in a representative orthogonal slit-pair.

Intuitively, Figure 1b demonstrates the design of metasurfaces with the superposition of tightly focused VBs of the orders $n = 1$ and $g = 3$, wherein panels I and II in Figure 1b are the inner and outer sets of slit-pairs of metasurface, respectively, for the VBs of smaller order $n = 1$ and the larger order $g = 3$; each set contains its own inner ring and outer ring of slits. Panel III is the metasurface interleaved with the two sets of slit-pair rings in maps I and II. The bottom row of each panel shows the distributions of intensities $|E_x|^2$ and $|E_y|^2$ of *x*- and *y*-components and the total intensity $|E_x|^2 + |E_y|^2$, respectively, for the VBs of orders 1 and 3 and the superimposed light fields.

Figure 1c shows the coordinate relations between the object plane and observation plane. Each set of slit-pairs is represented by two individual orthogonal slits. The radii of the inner and outer slits in each set are $r_q^{(i)}$ and $r_q^{(o)}$, where the subscript q taking n and g indicates the inner and outer set of slit-pairs respectively, as shown in Figure 1c, and the optical paths from the two slits to the origin O' of the observation plane are $s_q^{(i)}$ and $s_q^{(o)}$, respectively; they are expressed as $s_q^{(i)} = (r_q^{(i)\,2} + f^2)^{1/2}$ and $s_q^{(o)} = (r_q^{(o)\,2} + f^2)^{1/2}$. Furthermore, the optical path difference between the inner and outer ring slits to O' is $\lambda/2$, i.e., $s_q^{(o)} - s_q^{(i)} = \lambda/2$. In our design, the wavelength has taken $\lambda = 632.8$ nm, and the distance f from the object plane to the observation plane is set at $f = 5$ μm. Hereafter, the ring radius of a set of slit-pairs is signified by the radius of its inner-slit ring $r_q^{(i)}$, otherwise noted.

Figure 1d is the overlapped view of plane *Oxy* where the metasurface lies and plane *O′x′y′* for illustrating the coordinate relation of the object point $p\,(r, \theta)$ and the observation point $q\,(R, \alpha)$ with the distance ρ. Figure 1e is the diagram of a representative pair of slits at $p\,(r, \theta)$ with the geometrical quantities given in details. The length and width of each slit are $L = 250$ nm and $W = 80$ nm, respectively. The orientation angles of the long sides of the inner and outer slits with respect to *x* axis are φ and $\varphi + 90°$, respectively; φ is set as

$\varphi = \varphi_0 + m\theta$ to form a helical profile of geometric phase, where θ and m are the azimuthal angle and the rotational order of the slit-pair, respectively, and φ_0 denotes the orientation angle of the initial slit at $\theta = 0$. By setting $\varphi_0 = 0°$, it arrives at $\varphi = m\theta$, which is the case we use for the metasurface designs. Additionally, $\hat{e}_x$ and $\hat{e}_y$ are unit vectors in the x and y direction, $\hat{e}_r$ and $\hat{e}_t$ in radial and azimuthal directions, and $\hat{u}$ and $\hat{v}$ are in the directions parallel and perpendicular to the long side of the slit.

We first consider the wavefield excited at point p (r, θ) by an outer slit-pair of the metasurface. As shown in Figure 1e, the unit vectors $\hat{u}$ and $\hat{v}$ can be written as $\hat{u} = cos\varphi\hat{e}_x + \sin\varphi\hat{e}_y$ and $\hat{v} = -\sin\varphi\hat{e}_x + \cos\varphi\hat{e}_y$, respectively. It is known that the plasmonic field excited by a thin slit is perpendicular to long side of the slit [72], and it is along the direction of $\hat{v}$. Thus, when illuminated with circularly polarized light $E_{in}^{\sigma} = [1 \quad \sigma i]/\sqrt{2}$ with chirality σ, the transmitting wavefield E_v generated by the inner slit at p (r, θ) can be written as [61]

$$E_v = (E_{in}^{\sigma} \cdot \hat{v})\hat{v} = \frac{i\sigma}{\sqrt{2}} \exp(i\sigma\varphi)\hat{v}, \tag{1}$$

Similarly, the radial and azimuthal unit vector $\hat{e}_r$ and $\hat{e}_t$ are $\hat{e}_r = \cos\theta\hat{e}_x + \sin\theta\hat{e}_y$ and $\hat{e}_t = -\sin\theta\hat{e}_x + \cos\theta\hat{e}_y$ according to the geometric relation in Figure 1e, respectively. The radial and azimuthal components $E_{vr}^{(i)}$ and $E_{vt}^{(i)}$ of the wave field excited by this inner slit in $\hat{e}_r$ and $\hat{e}_t$ can be written as

$$E_{vr}^{(i)} = (E_v \cdot \hat{e}_r)\hat{e}_r = \frac{i\sigma}{\sqrt{2}} \exp(i\sigma\varphi)\sin(\theta - \varphi)\hat{e}_r, \tag{2}$$

$$E_{vt}^{(i)} = (E_v \cdot \hat{e}_t)\hat{e}_t = \frac{i\sigma}{\sqrt{2}} \exp(i\sigma\varphi)\cos(\theta - \varphi)\hat{e}_t, \tag{3}$$

By taking it into account that the orientation of the outer slit of a slit-pair is perpendicular to the inner slit, the radial and azimuthal components $E_{vr}^{(o)}$ and $E_{vt}^{(o)}$ of wavefield excited by the corresponding outer slit can be written as

$$E_{vr}^{(o)} = \frac{1}{\sqrt{2}} \exp(i\sigma\varphi)\cos(\theta - \varphi)\hat{e}_r, \tag{4}$$

$$E_{vt}^{(o)} = \frac{-1}{\sqrt{2}} \exp(i\sigma\varphi)\sin(\theta - \varphi)\hat{e}_t, \tag{5}$$

It is noted that the optical path difference δ between the two slits in a pair to a point in the area near the center O' results in the propagation phase $k\delta$, where $k = 2\pi/\lambda$ and $\delta = \lambda/2$; based on Equations (2)–(5), the radial and azimuthal components E_{pr} (r, θ) and E_{pt} (r, θ) of the wavefield produced by the slit-pair are obtained [73]:

$$E_{pr}(r, \theta) = E_{vr}^{(i)} + E_{vr}^{(o)} \exp(ik\delta) = \frac{-1}{\sqrt{2}} \exp[i\sigma(2\varphi - \theta)]\hat{e}_r, \tag{6}$$

$$E_{pt}(r, \theta) = E_{vt}^{(i)} + E_{vt}^{(o)} \exp(ik\delta) = \frac{i\sigma}{\sqrt{2}} \exp[i\sigma(2\varphi - \theta)]\hat{e}_t, \tag{7}$$

With the following transformation matrix:

$$\begin{bmatrix} E_{px}(r, \theta) \\ E_{py}(r, \theta) \end{bmatrix} = \begin{bmatrix} \cos\theta & -\sin\theta \\ \sin\theta & \cos\theta \end{bmatrix} \begin{bmatrix} E_{pr}(r, \theta) \\ E_{pt}(r, \theta) \end{bmatrix}, \tag{8}$$

and substituting (6) and (7) into (8), we obtain the wavefield in the Cartesian coordinates:

$$E_p^{\sigma}(r, \theta) = \frac{-1}{\sqrt{2}} \exp(i2\sigma m\theta) \begin{bmatrix} 1 \\ -\sigma i \end{bmatrix}, \tag{9}$$

From the above equation, it can be seen that the incident circular polarization of the chirality σ is converted to the opposite polarization of chirality $-\sigma$ for the field with the geometric phase $\exp(i2\sigma m\theta)$ imposed. This indicates that the slit-pair has the functionality of polarization conversion similar to a half-wave plate under the above given conditions [74].

Based on the Huygens-Fresnel principle of surface plasmons [75], the wavefield $E_g^\sigma(R,\alpha)$ at the point q (R,α) of observation plane is the superposition of the wavefields $E_p^\sigma(r,\theta)$ excited by all slit-pairs on the outer ring of the metasurface, and it is expressed as

$$E_g^\sigma(R,\alpha) = -i/\sqrt{\rho\lambda}\int E_p^\sigma(r,\theta)\exp[i(k\rho+\pi/4)]rd\theta,\tag{10}$$

In the area near the center point O', it holds that $R << r$, and thus the ρ is approximated as $\rho \approx s - Rr\cos(\theta-\alpha)/s$, wherein s is the distance from the point p (r,θ) to O', $s = (f^2+r^2)^{1/2}$. Remembering the orientation angle $\varphi = m\theta$ and using the properties of the Bessel function, the calculations on Equation (10) give the following expression:

$$E_g^\sigma(R,\alpha) = iC(-i)^{\sigma g}\exp(i\sigma g\alpha)J_{\sigma g}(kRr_g^{(i)}/s_g^{(i)})\begin{bmatrix}1\\-\sigma i\end{bmatrix},\tag{11}$$

where $r_g^{(i)} = r$, $s_g^{(i)} = s$, $g = 2m$, m is the rotational order of the slit-pairs, and $C = r_g^{(i)}/\sqrt{2\lambda f}\pi exp[i(ks_g^{(i)}+\pi/4)]$ is a complex constant. The above equation indicates that the slit-pairs on the outer ring produces an optical vortex of chirality $-\sigma$ opposite to the incident circular polarization with topological charge g; the radial intensity profile is the modulus square of the Bessel function $\left|J_{\sigma g}(kRr_g^{(i)}/s_g^{(i)})\right|^2$. Intuitively, under the illumination of left-handed circular polarization with $\sigma = 1$, the optical vortex of order g of right circular polarization will be produced and vice versa.

Furthermore, when the illuminating light is linearly polarized in the horizontal direction, it contains both the left and right circular polarizations $E_{in}^{\sigma=1}$ and $E_{in}^{\sigma=-1}$, and it is denoted as $E_{in}^L = E_{in}^{\sigma=1}+E_{in}^{\sigma=-1}$. Based on the above analysis and Equation (11), the light field E_g (R,α) produced by the set of slit-pairs on the outer ring is the superposition of the two circularly polarized vortices of topological charge $\pm g$:

$$E_g(R,\alpha) = E^{\sigma=1}(R,\alpha)+E^{\sigma=-1}(R,\alpha)$$

$$\propto (-i)^{g-1}J_g(kRr_g^{(i)}/s_g^{(i)})\begin{bmatrix}\cos g\alpha\\\sin g\alpha\end{bmatrix},\tag{12}$$

The above Equation shows that the set of slit-pairs produces a radial VB of order g, while the x- and y- component fields varies with $\cos g\alpha$ and $\sin g\alpha$, respectively.

Likewise, similar analysis and results also hold for the light field produced by the slit-pairs on the inner ring of the metasurface, and resultantly, under the illuminating light of horizontal linear polarization, the radial VB of order n with the form similar to Equation (12) is obtained, and the light field E_n (R,α) can be expressed as follows:

$$E_n(R,\alpha) \propto (-i)^{n-1}J_n(kRr_n^{(i)}/s_n^{(i)})\begin{bmatrix}\cos n\alpha\\\sin n\alpha\end{bmatrix},\tag{13}$$

Here, n is the rotational order of slit-pairs on the inner ring. Thus, as the superposition of the vector light fields E_n (R,α) and E_g (R,α), the light field E (R,α) produced by the entire metasurface is the following:

$$E(R,\alpha) = E_n(R,\alpha)+E_g(R,\alpha)$$

$$\propto \begin{bmatrix}(-i)^{n-1}J_n(kRr_n^{(i)}/s_n^{(i)})\cos n\alpha+(-i)^{g-1}J_g(kRr_g^{(i)}/s_g^{(i)})\cos g\alpha\\(-i)^{n-1}J_n(kRr_n^{(i)}/s_n^{(i)})\sin n\alpha+(-i)^{g-1}J_g(kRr_g^{(i)}/s_g^{(i)})\sin g\alpha\end{bmatrix}.\tag{14}$$

The above equation is the expression for the superimposed light field of profile-tunable tightly focused VBs of orders n and g, with the two components E_x and E_y given in Jones vector, respectively, and the corresponding intensities $|E_x|^2$ and $|E_y|^2$ and the total light intensity $|E_x|^2 + |E_y|^2$ are readily obtained.

Essentially, the optical path difference of $\lambda/2$ and the orthogonality of the two slits in a slit-pair introduce, respectively, the propagation phase and the geometrical phase of π, and their combination enables the light field near the center O' to be the superposition of constructive interference. Thus, the wavelets from all slit-pairs on an entire ring produces the same effect as focusing; with the rotational order of the slit-pair taken into account, a focused vortex field is formed in the central area near O'. Moreover, the set focal length for the constructive interference is $f = 5$ μm, being of the same order as the radius of the slit-pair ring, and such setting corresponds to a larger numerical aperture of focusing. Therefore, the radial VBs of orders n and g may have the spot sizes of the component E_z smaller than a resolution limit (0.61λ/N.A.), and the two VBs can be regarded as tightly focused. Consequently, the superposition of tightly focused VBs can be realized. Based on Equation (14), it can be also deduced that the radius R_n and R_g of the doughnut intensity profiles of the two VBs are related to the first maximum points X_n and X_g for the Bessel functions of the orders n and g, respectively, with $X_n = kR_n r_n^{(i)}/s_n^{(i)}$ and $X_g = kR_g r_g^{(i)}/s_g^{(i)}$. Yet, for the superposition of traditional Bessel VBs, it can be considered as the case in which the radius $r_n^{(i)}$ and $r_g^{(i)}$ of the two slit-pair rings are equal; whereas the higher the order of Bessel VB, the larger the maximum point X_n or X_g and the larger the radius R_n or R_g of the doughnut. Different from conventional VBs, here by adjusting radii $r_n^{(i)}$ and $r_g^{(i)}$ of the slit-pair rings in accordance with the given rotation orders, respectively, the radii R_n and R_g of the doughnuts are modulated to be equal for the two generated VBs, i.e., $R_n = R_g$; thus, the superposition of the tightly focused VBs of profile tunability is finally realized, and the related structured light is also generated.

3. Theoretical Calculation and Numerical Simulation

3.1. Design of the Metasurfaces

According to the previous analysis and the geometric relation in Figure 1c, it is clear that the radii $r_q^{(i)}$ and $r_q^{(o)}$ of the inner and outer rings of a set of slit-pairs satisfy $r_q^{(o)} = [r_q^{(i)\,2} + \lambda^2/4 + \lambda(r_q^{(i)\,2} + f^2)^{1/2}]^{1/2}$, in addition, based on the above expressions $X_n = kR_n r_n^{(i)}/s_n^{(i)}$ and $X_g = kR_g r_g^{(i)}/s_g^{(i)}$ of the first maximum points for the Bessel functions of the orders n and g, the corresponding radius of the VB doughnut of order q could be written as $R_q = X_q(r_q^{(i)\,2} + f^2)^{1/2}/kr_q^{(i)}$, where X_q is the first maximum point for the Bessel function of order q, which gives the relation between the radius R_q of the doughnut and the radius $r_q^{(i)}$ of slit-pair ring. From this relation, the variation of the doughnut radius R_q of the VBs of order 1 to 4 versus $r_q^{(i)}$ is obtained and is shown in Figure 2a. If the doughnut radius of the two VBs to be superimposed are both set as R_s, by drawing the horizontal dashed line with vertical coordinate value of R_s as shown in Figure 2a, the horizontal coordinate of its intersections with the curves gives the radius of the corresponding slit-pair ring. We choose two of these intersection points labeled in red and blue, and we can read the radius $r_n^{(i)}$ and $r_g^{(i)}$ of the inner and outer slit-pair rings for $n = 1$ and $g = 3$, respectively; accordingly, the corresponding radii $r_n^{(o)}$ and $r_g^{(o)}$ of the outer slit rings in each slit-pair rings are also obtained through simple calculations. Thus, by achieving the radius values of the two slit-pair rings with the setting rotational orders, the metasurface for the superposition of profile-tunable VBs of order n and g is designed. In addition, in Figure 2a, the intersections of the vertical dashed line with the blue and red curves represents the equal radius $r_n^{(i)} = r_g^{(i)}$ of the two slit-pair rings with different rotation orders, and the corresponding doughnut radius values of R_s and R'_s are for the usual VB of unmodulated intensity profiles and their superposition.
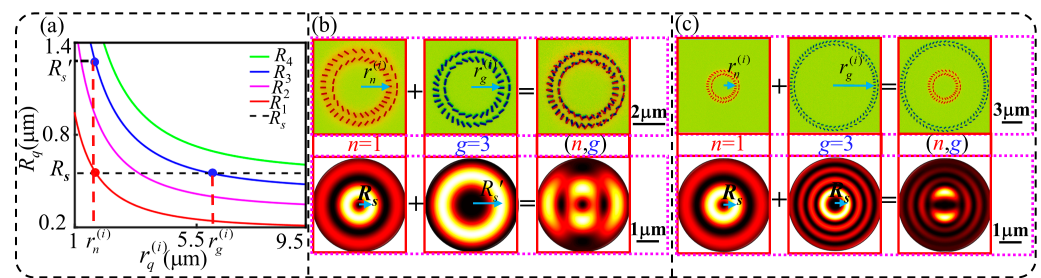
Figure 2. (**a**) The variation of the doughnut radius R_q for the VBs of orders 1 to 4 versus the radius $r_q^{(i)}$ of the slit-pair ring. Superposition of VBs of the orders 1 and 3 (**b**) by two slit-pair rings of equal radius but with unequal radii of the formed doughnuts and (**c**) by two slit-pair rings of modulated radius with equal radii of doughnuts.

In Figure 2b, the patterns from left to right in the upper row show the two slit-pair rings with the equal radius and the formed meature surface, respectively; the images in the lower row show the corresponding doughnuts and superimposed total intensity profile for VBs of order of 1 and 3, respectively. In contrast, Figure 2c shows in the upper row the inner and outer slit-pair rings with different radii $r_n^{(i)}$ and $r_g^{(i)}$ and the formed metasurface; the lower row are the images of the total intensity profiles for the two VBs with the same doughnut radius R_s and the superimposed fields, respectively. Compared with the results in Figure 2b, the results in Figure 2c for the superimposed fields of the profile-tunable VBs with equal doughnuts have different characteristics from the those of unmodulated VBs, and the intensity profile exhibits a simple pattern and concentrating power.

3.2. Calculation of the Superimposed Field of Tightly-Focused VBs

We practically designed four metasurface samples S_1, S_2, S_3 and S_4, to realize the superposition of profile-tunable tightly focused VBs of the orders $(n, g) = (1, 3)$, $(2, 4)$, $(1, 2)$ and $(2, 3)$, respectively. We first performed theoretical calculation of the light fields generated by each of the four samples based on the Huygens-Fresnel principle, and then implemented numerical simulation by using the finite difference in time domain (FDTD) for the superimposed fields and intensities. In the simulation, the parameters for the optical system and the metasurfaces are the same as those given in Section 2. For the designed metasurface, the Au film is 200 nm thick. The incident light is linearly polarized in the horizontal direction; it illuminates the metasurface from the side of substrate, and the output fields are calculated on the focused plane. The radii $r_n^{(i)}$ and $r_g^{(i)}$ of the two slit-pair rings were originally set with the theoretical values and were finely adjusted according to the practical results of FDTD simulations. The practical radius values for the inner and outer slit-pair rings of the metasurface samples and the corresponding doughnut-radius values of R_s are given in Table 1. In addition, we note that the complex refractive index of gold film is $0.12517 + 3.3326\,i$ and the refractive index of SiO_2 is 1.4570 at wavelength 632.8 nm [76–78], as given in Table 2.

Table 1. Parameters of designed four samples (the two VBs of orders *n* and g to be superimposed have the equal doughnut radius R_s).
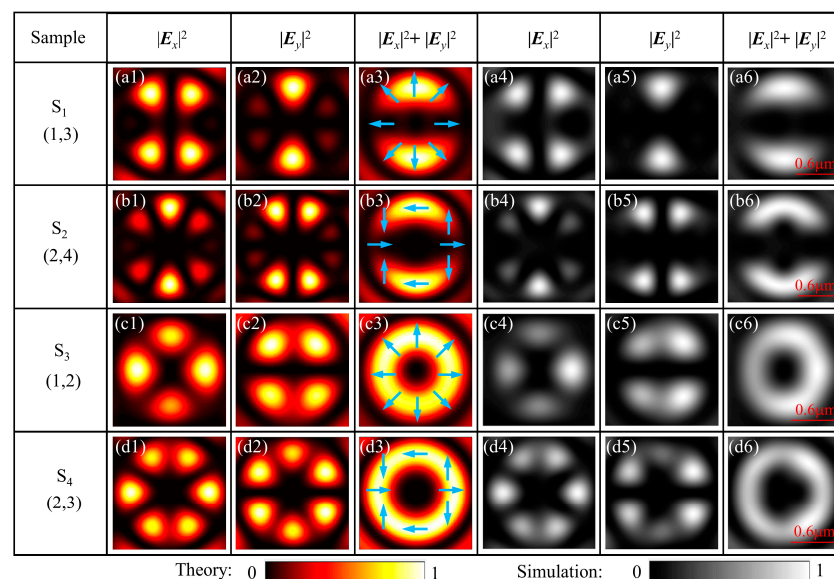
Sample	S_1	S_2	S_3	S_4
(n, g)	(1, 3)	(2, 4)	(1, 2)	(2, 3)
R_s	0.5458	0.63	0.432	0.4844
$r_n^{(i)}$	1.807	2.7983	2.3775	4.1119
$r_n^{(o)}$	2.587	3.3993	3.041	4.5939
$r_g^{(i)}$	6.048	8.0784	5.0731	8.978
$r_g^{(o)}$	6.448	8.4482	5.5085	9.3415

Table 2. Parameters of materials.

| Parameters	Gold Film	SiO$_2$ Substrate
thickness	200 nm	1 mm
Refrative index [76–78]	0.12517	1.457
Extinction coefficient [76–78]	3.3326	0

Figure 3 shows the theoretical and simulational intensity images of the superimposed profile-tunable VBs for samples S$_1$, S$_2$, S$_3$ and S$_4$, respectively. Figure 3(a1–d1,a2–d2,a3–d3) are the theoretical results for the *x*- and *y*- component and total intensities $|E_x|^2$, $|E_y|^2$ and $|E_x|^2 + |E_y|^2$ of the four samples, respectively; the overlaid blue arrows denote the polarization states of light fields. Figure 3(a4–d4,a5–d5,a6–d6) are the corresponding results of FDTD simulations, respectively. It can be seen that these intensity images have unique and interesting characteristics; particularly, for the superimposed fields of VBs of the orders 1 and 3 by samples S$_1$ and the orders 2 and 4 by S$_2$, respectively, the total light intensities $|E_x|^2 + |E_y|^2$ both show a unique double petal pattern, while patterns of the component intensities $|E_x|^2$ and $|E_y|^2$ have petals of variable numbers. These petal-shaped intensity distributions are not only different from those of the conventional single VBs [79], but also different from the superimposed fields of the VBs with unmodulated doughnuts [80] while for the superimposed fields of VBs of the orders 1 and 2 by samples S$_3$ and the orders 2 and 3 by S$_4$, respectively, the total intensity $|E_x|^2 + |E_y|^2$ still exhibits the well doughnut-shaped distribution. The component intensities $|E_x|^2$ and $|E_y|^2$ of the superimposed fields are apparently similar to those of the single VB of the order 2 and 3, respectively, which indicates that the VB of the higher order plays the dominant role in the superposition in the case when the order difference of two VBs is 1. Furthermore, we find it very interesting that for samples S$_1$ and S$_3$, the intensity distributions are entirely different from the VB of the order 1, but their spatial distributions of polarization are the same and are identical to the radially polarized VB of the order 1. Similarly, for samples S$_2$ and S$_4$, the intensity profiles are completely different from those of the VB of the order 2, but the distributions of polarizations are coincidentally the same as radially polarized VB of the order 2. This might be an example of inconsistent topologies in polarization singularity and helicity of the wavefronts in the superimposed VB fields.

Figure 3. The theoretical and simulation results for the intensities of the *x*- and *y*- components and total intensities $|E_x|^2$, $|E_y|^2$ and $|E_x|^2 + |E_y|^2$ of the superimposed VBs with equal doughnuts for the samples S$_1$, S$_2$, S$_3$ and S$_4$, respectively.

3.3. Analysis of Results

For more detailed analysis of the characteristics of the superimposed fields, Figure 4 shows the curves of the component and total intensities versus azimuthal angle α for the four samples where each intensity curve is taken at the radius of the doughnut corresponding to the first maximum value of the Bessel functions. The black, green and blue curves in the figures show the component intensities $|E_x|^2$ and $|E_y|^2$ and total intensity $|E_x|^2 + |E_y|^2$, respectively. We take sample S_1 as an example to analyze the intensity curves, in which the two VBs involved in generating the superimposed fields are of orders 1 and 3, respectively. From the x- and y- components E_x and E_y of the superimposed fields given in Equation (14), the corresponding component and total intensities are $|E_x|_2 = J_{1M}^2 \cos^2\alpha + J_{3M}^2 \cos^2 3\alpha - 2J_{1M}J_{3M}\cos\alpha\cos 3\alpha$, $|E_y|_2 = J_{1M}^2 \sin^2\alpha + J_{3M}^2 \sin^2 3\alpha - 2J_{1M}J_{3M}\sin\alpha\sin 3\alpha$ and $|E|_2 = J_{1M}^2 + J_{3M}^2 - 2J_{1M}J_{3M}\cos 2\alpha$, respectively. Here J_{1M} and J_{3M} are the first maxima of Bessel functions of orders 1 and 3, respectively.
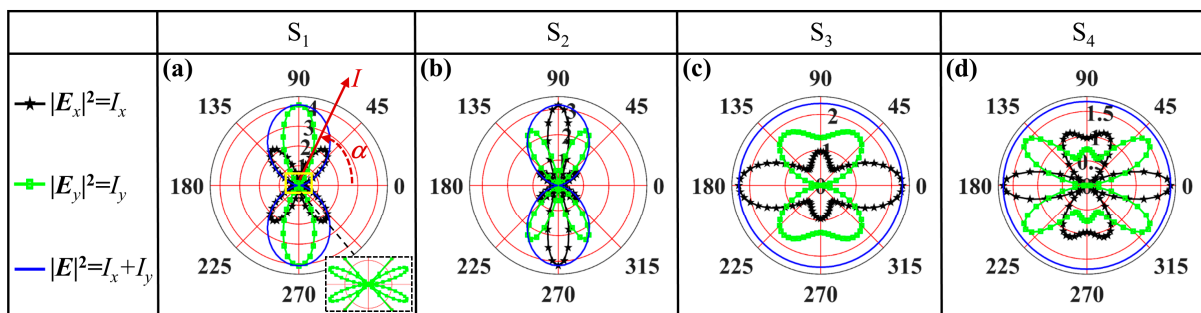
Figure 4. The curves of the intensity of superimposed VBs versus azimuthal angle α, (**a–d**) show the theoretical curves of the intensities $|E_x|^2$, $|E_y|^2$ and $|E_x|^2 + |E_y|^2$ with α for samples S_1–S_4, respectively.

These results are demonstrated by the intensity curves of the superimposed VBs of orders 1 and 3 in Figure 4a. According to the above expressions, $|E|^2$ takes the maxima at $\alpha = 90°$ and $270°$, which is in consistency with the two bright petals in the theoretical and simulation intensity patterns in Figure 3(a3,a6), respectively. For the expression of $|E_x|^2$, the maxima of intensity are at $\alpha = 53.0°$, $127.0°$, $233.0°$ and $307.0°$, which conforms with the four bright petals of the intensities in Figure 3(a1,a4), while for the expression of $|E_y|^2$, two major maxima appear at $\alpha = 90°$ and $270°$, which are verified by the curves in Figure 4a; interestingly, four minor maxima also appear at $\alpha \approx 21.7°$, $158.2°$, $201.8°$ and $338.3°$, which are demonstrated in the inset of Figure 4a as the magnified view of the central part of the curve $I = |E_y|^2$ and are also observed in both the theoretical and simulation patterns in Figure 3(a2,a5). Coincidentally, the superimposed field of the VBs of orders 2 and 4 by sample S_2 has the similar characteristics, and the curves of the intensity versus α in Figure 4b are consistent with the theoretical and simulation results in Figure 3(b1–b6).

In contrast, for the superimposed fields of VBs of the orders 1 and 2 by samples S_3 and the orders 3 and 4 by S_4, the intensity distributions have the common characteristics. Similarly, taking sample S_3 as the example, we obtain that $E_x \propto J_{1M}\cos\alpha - iJ_{2M}\cos 2\alpha$ and $E_y \propto J_{1M}\sin\alpha - iJ_{2M}\sin 2\alpha$; the corresponding intensities are $|E_x|_2 = J_{1M}^2\cos^2\alpha + J_{2M}^2\cos^2 2\alpha$, $|E_y|_2 = J_{1M}^2\sin^2\alpha + J_{2M}^2\sin^2 2\alpha$ and $|E|_2 = J_{1M}^2 + J_{2M}^2$. These expressions correspond to the intensity curves versus α for sample S_3 in Figure 4c; it is interesting that the curve of the total intensity $|E|^2$ is of constant value, as indicated by circle of constant radius $J_{1M}^2 + J_{2M}^2$, which is supported by the homogeneous doughnut distributions in Figure 3(c3,c6). In addition, $|E_x|^2$ takes the major maxima at $\alpha = 0°$ and $180°$, and the minor maxima at $\alpha = 90°$ and $270°$, and $|E_y|^2$ takes the maxima at $\alpha \approx 55.2°$, $124.7°$, $235.2°$ and $304.7°$, as demonstrated in the corresponding curve in Figure 4c. Apparently, these features are consistent with the theoretical and simulation patterns for sample S_3 in Figure 3(c1–c6).

On the whole, for the superposition of VBs of the orders $n = 1$ and $g = 3$ by samples S_1 and for that of the orders 2 and 4 by S_2, respectively, the double petals in the total intensity are originated from the cross term $-2J_n J_g \cos(g - n)\alpha$, which causes the

maxima at $\alpha = 90°$ and $270°$. Similarly, the cross terms also provide diverse petal distributions for the intensities of the component fields. However, for the superposition of VBs of orders $n = 1$ and $g = 2$ and VBs of orders 2 and 3 by samples S_3 and S_4, respectively, the cross terms are vanished owing to the orthogonality of the real and imaginary parts in the VB fields, and total intensities are reduced to the incoherent additions of the VB intensities. Thus, the doughnuts of the total intensities appear to be homogeneous. Additionally, as the cosine or sine function squared of α, the intensities of the VBs of higher orders vary more rapidly versus α; thereby the component intensities of sample S_3 and S_4 exhibit the distributions with more petals, very much similar to the involved higher-order VB in the superposition. Here we note that these phenomena are unique in the superimposed fields of tightly focused VBs with equal doughnuts in this work, and they would enrich the structured light fields with novel constituents.
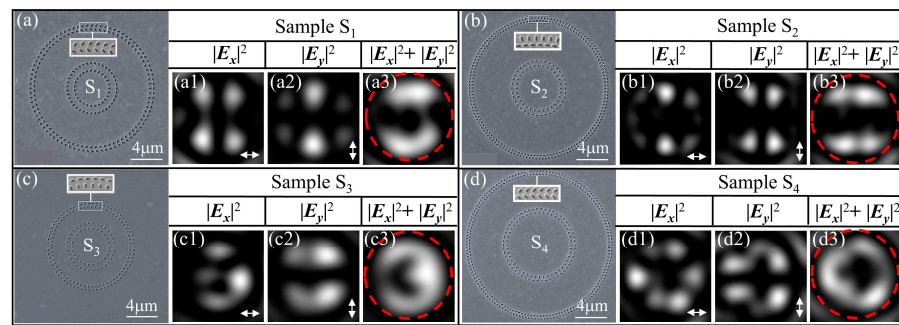
4. Experiment

Figure 5 shows the optical setup constructed for measuring the superimposed light field of the profile-tunable tightly focused VBs. The He-Ne laser emits a vertically, linearly polarized light beam with the wavelength of 632.8 nm, and a half-wave plate (HWP) is used to adjust the polarization of the incident light. To match the designed metasurface samples, the incident light is adjusted to be horizontally, linearly polarized; and it illuminates the sample from the side of the SiO_2 substrate, which is placed on the three-dimensional translation stage. The microscopic objective lens (MO, N.A. = 0.9/100×) is used to magnify and image the superimposed field, which is obtained at 5 μm from the sample surface. Then the image intensity pattern is captured by the sCMOS (Zyla-5.5, 16) placed on the image plane. An analyzing polarizer (P) is used to extract the light intensities $|E_x|^2$ and $|E_y|^2$ of the x and y components of the superimposed fields. The quarter-wave plate (QWP) is typically removed from the optical path; when it is placed in, the setup will be used to measure the superimposed fields of the profile-tunable higher-order Poincaré VBs, which will be discussed in the following section.
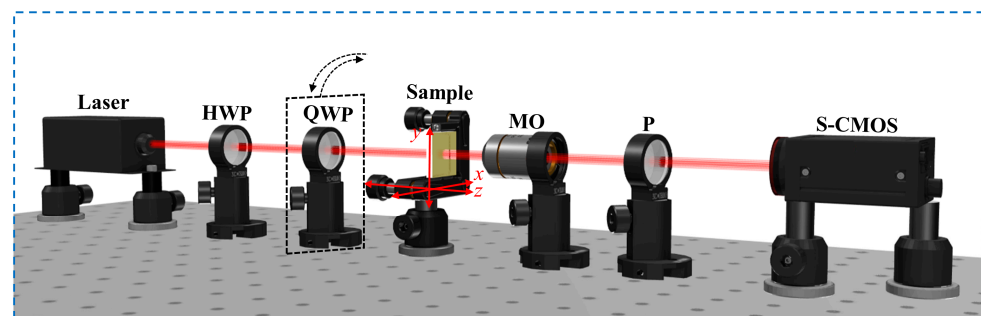
Figure 5. The diagram of experimental optical setup. From left to right, the optical devices including the laser, half-wave plate (HWP), quarter-wave plate (QWP), sample and three-dimensional translation stage, microscopic objective lens (MO), analytical polarizer (P), and sCMOS camera are shown.

In the fabrication of the metasurface sample, the Au film with a thickness of 200 nm was deposited on the SiO_2 substrate by magnetron sputtering, and then two sets of orthogonal slit-pairs were etched in the gold film with the focused ion beam (FIB) system (FEI Helios G4 UX) with the resolution 4.0 nm at 30 kV using the preferred statistical method. The radius parameters of the slit-pair rings for the fabricated samples S_1, S_2, S_3 and S_4 are the same as those in Table 1, and the nanoslit parameters are the same as those in the FDTD simulations. Again, the four fabricated samples are used to generate the superimposed fields of the VBs of the orders $(n, g) = (1, 3)$, $(2, 4)$, $(1, 2)$ and $(2, 3)$, respectively. Figure 6a–d are the SEM images of samples S_1–S_4, respectively, and the insets show the local magnified views. From the variation of the orientation angles of the nanoslits in the images, the rotational orders of the two sets of slit-pairs $(n/2, g/2) = (0.5, 1.5)$, $(1, 2)$, $(0.5, 1)$ and $(1, 1.5)$ could be qualitatively

judged for the four samples, respectively. Figure 6(a1–d1,a2–d2,a3–d3) are the images of the component and total intensities $|E_x|^2$, $|E_y|^2$ and $|E_x|^2 + |E_y|^2$ generated by samples S$_1$–S$_4$, respectively. On the whole, they are in agreement with the corresponding theoretical and simulation results in Figure 3, validating feasibility of the method for metasurface designs. It should also be noted that there are still some discrepancies between the experimental and theoretical results. These discrepancies mainly stem from the unavoidable factors, such as the errors of nanoslit sizes in the fabrications, the imperfectness of optical elements, and misalignment in the optical setup for the measurements, which may deteriorate the quality of the intensity images in the experiments. In addition, there is a small amount of residual gallium ions on the samples fabricated with FIB; however, the surface plasmon polaritons (SPPs) excited by gallium ions are usually much weaker than those excited by noble metals or gold. So, the errors of the optical fields caused by the residual gallium ions might be much smaller than those due to the several factors as mentioned above, and then the influence of the residual gallium ions might be very insignificant. We believe that such interesting experimental phenomena are of potential applications in the fields such as optical communications, particle manipulations and quantum information.

Figure 6. SEM images of the four samples and the experimental intensity images of the superimposed VBs. The insets show the magnified local images of the orthogonal slit-pairs.

5. Discussions

In the above, the polarization states of the VBs produced by each set of slit-pairs in the metasurface are linearly polarized, and it is the fundamental case in the generation of VBs. In fact, compared with the linearly polarized VBs, the higher-order Poincaré (HOP) VBs with elliptical polarizations are more generalized and have wider applications. As well understood, the spatially variant polarization states of the HOP VB are represented by a point on the HOP sphere [81]. By adjusting the ellipticity of the illumination light in our experiment, the four metasurface samples can be extended to realize the superposition of profile-tunable HOP VBs, with the resultant structured light fields being achieved correspondingly. The elliptically polarized incident light E_{in} can be represented by the point (2Θ, 2Φ) on the conventional Poincaré sphere, and it is written as

$$E_{in} = \sum_{\sigma=-1(\sigma\neq0)}^{1} a_\sigma \exp(-i\sigma\Phi)E_{in}^\sigma, \tag{15}$$

where the normalized amplitude a_σ is expressed as $a_{\sigma=1} = \sin\Theta$ and $a_{\sigma=-1} = \cos\Theta$ for $\sigma = 1$ and $\sigma = -1$, respectively. Using the above Equation and following the derivations of E_g (R, α) in Equations (11) and (12), we derive the light field $E_g^{(e)}(R, \alpha)$ produced by the slit-pairs on the outer ring under the illumination of elliptical polarization, in which the circular polarization $E_{in}^\sigma = [1 \quad \sigma i]/\sqrt{2}$ were replaced by $a_\sigma \exp(-i\sigma\Phi) E^\sigma$ for both $\sigma = 1$ and $\sigma = -1$; then we obtain

$$E_g^{(e)}(R, \alpha) \propto \sum_{\sigma=-1(\sigma\neq0)}^{1} a_\sigma(-i)^{\sigma g-1} J_l(kRr_g^{(i)}/s_g^{(i)}) \begin{bmatrix} 1 \\ -\sigma i \end{bmatrix} \exp[i\sigma(g\alpha - \Phi)], \tag{16}$$

where $l = \sigma q$ signifies the order of Bessel function, with q taking either g or n for the outer or inner slit-pairs rings. Similarly, for the slit-pairs on inner ring of the metasurface, the HOP VB $\boldsymbol{E}_n^{(e)}(R, \alpha)$ is written as

$$\boldsymbol{E}_n^{(e)}(R, \alpha) \propto \sum_{\sigma=-1(\sigma \neq 0)}^{1} a_\sigma (-i)^{\sigma n - 1} J_l(kRr_n^{(i)}/s_g^{(i)}) \begin{bmatrix} 1 \\ -\sigma i \end{bmatrix} \exp[i\sigma(n\alpha - \Phi)], \qquad (17)$$

Consequently, the superimposed light fields $\boldsymbol{E}^{(e)}(R, \alpha)$ of the HOP VBs of the orders n and g are written as

$$\boldsymbol{E}^{(e)}(R, \alpha) = \boldsymbol{E}_n^{(e)}(R, \alpha) + \boldsymbol{E}_g^{(e)}(R, \alpha)$$

$$\propto \sum_{q=n,g} \sum_{\sigma=-1(\sigma \neq 0)}^{1} a_\sigma (-i)^{\sigma q - 1} J_l(kRr_q^{(i)}/s_q^{(i)}) \begin{bmatrix} 1 \\ -\sigma i \end{bmatrix} \exp[i\sigma(q\alpha - \Phi)], \qquad (18)$$

By changing the elliptical polarization of the illuminating light to adjust its position $(2\Theta, 2\Phi)$ on the conventional Poincaré sphere, the designed metasurfaces realize the superposition of HOP VBs $\boldsymbol{E}_n^{(e)}$ and $\boldsymbol{E}_g^{(e)}$ with equal doughnut size. Here we notice that $\boldsymbol{E}_n^{(e)}$ and $\boldsymbol{E}_g^{(e)}$ are at the points with same spherical coordinates $(2\Theta, 2\Phi)$ but on the HOP spheres of orders n and g, respectively. In the left and right parts in Figure 7a, the two HOP spheres of the orders n and g are drawn, respectively, and on each sphere, the nine points i to ix are labeled on each sphere from the north pole to the south pole along the prime meridian of $\Phi = 0$. In the middle part of Figure 7a, the schematic is drawn for the superimposed HOP vector light fields $\boldsymbol{E}_{n,\,\mathrm{i}}^{(e)} + \boldsymbol{E}_{g,\,\mathrm{i}}^{(e)}$ to $\boldsymbol{E}_{n,\,\mathrm{ix}}^{(e)} + \boldsymbol{E}_{g,\,\mathrm{ix}}^{(e)}$ of the tightly focused VBs. While the north and south poles on each HOP sphere represent the left and right circularly polarized optical vortices, respectively, the point on the equator represents the linearly polarized vector light field and the other points on the HOP sphere represent the HOP fields of elliptical polarizations.

In the experimental measurements, we also used the setup in Figure 5 but moved the QWP into the optical path; by combining the HWP and QWP to adjust the ellipticity of the incident light, the superposition of the HOP vector fields at the above nine points was realized. Figure 7b shows the experimental and simulation images of the superimposed HOP VBs for samples S_1 and S_3, where the arrowed circle, ellipses and line in the upper title row indicate the polarization states corresponding to points i to ix on the conventional Poincaré sphere. The gray-scale images in rows A, C and E are the experimental intensity profiles for $|E_x|^2$ and $|E_y|^2$ and $|E_x|^2 + |E_y|^2$ of the superimposed fields produced by sample S_1, respectively; the images in rows F, H and J are the corresponding experimental results of intensities by sample S_3, respectively; and the colored images in rows B, D, G and I are the corresponding simulation counterparts to the experimental images, respectively, as labeled by the color bars; the double-arrowed lines in the left title column labels the transmitting direction of the analyzing polarizer. It can be seen that when the polarization state changes from that in column i to column ix, the boundary of the petals in intensity profiles changes from being blurred to being clear and then to being blurred again. Moreover, in the results for sample S_3, the light intensity profiles undergo a rotation. The phenomena are related to the varying amplitudes of the left-handed and right-handed circularly polarized vortices in HOP VBs of orders n and g during the change of the incident polarization ellipticity. Apparently, for the polarization states at two symmetrical points with respect to the equator, the amplitude and phase of the left-handed and right-handed circularly polarized vortices are flipped, and this leads to the conversion of y components in the superposed fields; as a result, the intensity profiles appear to be rotating with evolution of the polarization states on the prime meridian. We believe that the superposition of profile-tunable tightly focused HOP VBs would be of significance for applications in fields such as quantum communications and cryptography, optical trapping and vector mode multiplexing.
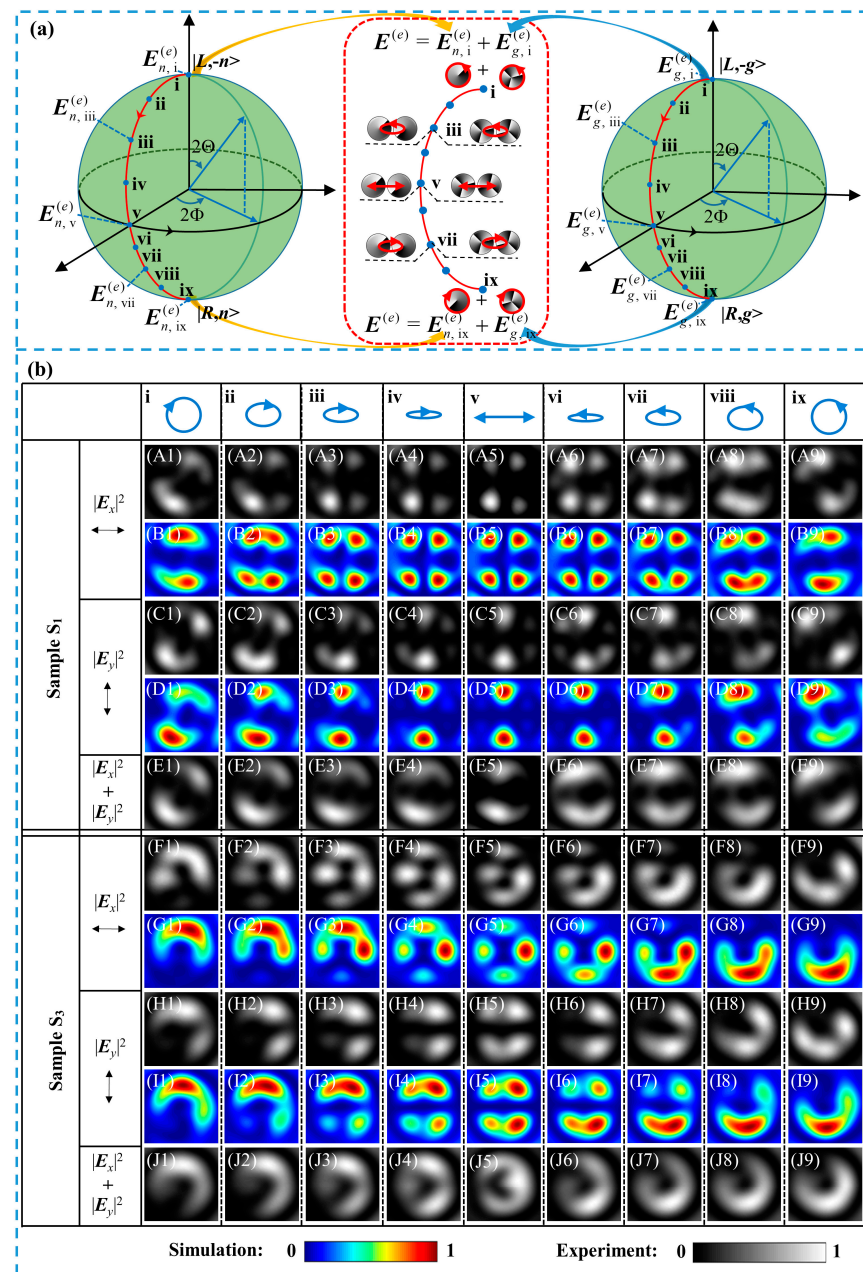
Figure 7. (**a**) The left panel: the HOP spheres of order *n*; the right panel: HOP spheres of order *g*; middle panel: the illustration of the superposition of the two HOP VBs. (**b**) Experimental and simulation intensities $|E_x|^2$, $|E_y|^2$ and $|E_x|^2 + |E_y|^2$ of the superimposed light fields for the HOP VBs of the order *n* and *g* with equal doughnut size produced by samples S$_1$ and S$_3$, respectively.

6. Conclusions

In conclusion, by spatially multiplexing the orthogonal nano-slit pairs on rings, we propose a metasurface to realize the superposition of profile-tunable tightly focused VBs and the generation of the corresponding structured light fields. By setting the rotational orders of the slit-pairs and by adjusting the radii of both inner and outer rings of the slit-pairs in the metasurface, the intensity profiles of two arbitrary-order VBs are modulated to have the doughnuts of equal sizes, and the superimposed fields are achieved. Furthermore, by changing the elliptical polarizations of the incident light, the superposition of the profile-tunable HOP VBs was also realized. We expect that this research will contribute to the literature of manipulating VBs and generating novel structured light fields. It would also be

of great significance to potential applications such as particle trapping, optical encryption, and optical communications with high capacities.

Institutional Review Board Statement: Not applicable.

Informed Consent Statement: Not applicable.

Data Availability Statement: Data are contained within the article.

Conflicts of Interest: The authors declare no conflict of interest.

References

1. Chen, W.T.; Zhu, A.Y.; Capasso, F. Flat optics with dispersion-engineered metasurfaces. *Nat. Rev. Mater.* **2020**, *5*, 604–620. [CrossRef]
2. Ding, F.; Yang, Y.; Deshpande, R.A.; Bozhevolnyi, S.I. A review of gap-surface plasmon metasurfaces: Fundamentals and applications. *Nanophotonics* **2018**, *7*, 1129–1156. [CrossRef]
3. Li, A.; Singh, S.; Sievenpiper, D. Metasurfaces and their applications. *Nanophotonics* **2018**, *7*, 989–1011. [CrossRef]
4. Zang, X.; Ding, H.; Intaravanne, Y.; Chen, L.; Peng, Y.; Xie, J.; Ke, Q.; Balakin, A.V.; Shkurinov, A.P.; Chen, X.; et al. A Multi-Foci Metalens with Polarization-Rotated Focal Points. *Laser Photonics Rev.* **2019**, *13*, 1900182. [CrossRef]
5. Chen, M.K.; Wu, Y.; Feng, L.; Fan, Q.; Lu, M.; Xu, T.; Tsai, D.P. Principles, Functions, and Applications of Optical Meta-Lens. *Adv. Opt. Mater.* **2021**, *9*, 2001414. [CrossRef]
6. Khorasaninejad, M.; Chen, W.T.; Devlin, R.C.; Oh, J.; Zhu, A.Y.; Capasso, F. Metalenses at visible wavelengths: Diffraction-limited focusing and subwavelength resolution imaging. *Science* **2016**, *352*, 1190–1194. [CrossRef]
7. Zhao, R.; Sain, B.; Wei, Q.; Tang, C.; Li, X.; Weiss, T.; Huang, L.; Wang, Y.; Zentgraf, T. Multichannel vectorial holographic display and encryption. *Light Sci. Appl.* **2018**, *7*, 95. [CrossRef]
8. Ren, H.; Briere, G.; Fang, X.; Ni, P.; Sawant, R.; Héron, S.; Chenot, S.; Vézian, S.; Damilano, B.; Brändli, V.; et al. Metasurface orbital angular momentum holography. *Nat. Commun.* **2019**, *10*, 2986. [CrossRef]
9. Kim, I.; Jang, J.; Kim, G.; Lee, J.; Badloe, T.; Mun, J.; Rho, J. Pixelated bifunctional metasurface-driven dynamic vectorial holographic color prints for photonic security platform. *Nat. Commun.* **2021**, *12*, 3614. [CrossRef]
10. Ren, H.; Fang, X.; Jang, J.; Bürger, J.; Rho, J.; Maier, S.A. Complex-amplitude metasurface-based orbital angular momentum holography in momentum space. *Nat. Nanotechnol.* **2020**, *15*, 948–955. [CrossRef]
11. Tseng, M.L.; Jahani, Y.; Leitis, A.; Altug, H. Dielectric Metasurfaces Enabling Advanced Optical Biosensors. *ACS Photonics* **2021**, *8*, 47–60. [CrossRef]
12. Zhang, S.; Wong, C.L.; Zeng, S.; Bi, R.; Tai, K.; Dholakia, K.; Olivo, M. Metasurfaces for biomedical applications: Imaging and sensing from a nanophotonics perspective. *Nanophotonics* **2021**, *10*, 259–293. [CrossRef]
13. Kim, I.; Martins, R.J.; Jang, J.; Badloe, T.; Khadir, S.; Jung, H.-Y.; Kim, H.; Kim, J.; Genevet, P.; Rho, J. Nanophotonics for light detection and ranging technology. *Nat. Nanotechnol.* **2021**, *16*, 508–524. [CrossRef] [PubMed]
14. Rodrigo, D.; Tittl, A.; Ait-Bouziad, N.; John-Herpin, A.; Limaj, O.; Kelly, C.; Yoo, D.; Wittenberg, N.J.; Oh, S.-H.; Lashuel, H.A.; et al. Resolving molecule-specific information in dynamic lipid membrane processes with multi-resonant infrared metasurfaces. *Nat. Commun.* **2018**, *9*, 2160. [CrossRef] [PubMed]
15. Flauraud, V.; Reyes, M.; Paniagua-Domínguez, R.; Kuznetsov, A.I.; Brugger, J. Silicon Nanostructures for Bright Field Full Color Prints. *ACS Photonics* **2017**, *4*, 1913–1919. [CrossRef]
16. Daqiqeh Rezaei, S.; Dong, Z.; You En Chan, J.; Trisno, J.; Ng, R.J.H.; Ruan, Q.; Qiu, C.-W.; Mortensen, N.A.; Yang, J.K.W. Nanophotonic Structural Colors. *ACS Photonics* **2021**, *8*, 18–33. [CrossRef]
17. Sun, S.; Zhou, Z.; Zhang, C.; Gao, Y.; Duan, Z.; Xiao, S.; Song, Q. All-Dielectric Full-Color Printing with TiO$_2$ Metasurfaces. *ACS Nano* **2017**, *11*, 4445–4452. [CrossRef]
18. Yang, W.; Xiao, S.; Song, Q.; Liu, Y.; Wu, Y.; Wang, S.; Yu, J.; Han, J.; Tsai, D.-P. All-dielectric metasurface for high-performance structural color. *Nat. Commun.* **2020**, *11*, 1864. [CrossRef]
19. Sun, S.; Yang, K.-Y.; Wang, C.-M.; Juan, T.-K.; Chen, W.T.; Liao, C.Y.; He, Q.; Xiao, S.; Kung, W.-T.; Guo, G.-Y.; et al. High-Efficiency Broadband Anomalous Reflection by Gradient Meta-Surfaces. *Nano Lett.* **2012**, *12*, 6223–6229. [CrossRef]

20.　Lin, D.; Fan, P.; Hasman, E.; Brongersma, M.L. Dielectric gradient metasurface optical elements. *Science* **2014**, *345*, 298–302. [CrossRef]

21.　Yu, N.; Genevet, P.; Kats, M.A.; Aieta, F.; Tetienne, J.-P.; Capasso, F.; Gaburro, Z. Light Propagation with Phase Discontinuities: Generalized Laws of Reflection and Refraction. *Science* **2011**, *334*, 333–337. [CrossRef]

22.　Sun, S.; He, Q.; Xiao, S.; Xu, Q.; Li, X.; Zhou, L. Gradient-index meta-surfaces as a bridge linking propagating waves and surface waves. *Nat. Mater.* **2012**, *11*, 426–431. [CrossRef] [PubMed]

23.　Huang, L.; Chen, X.; Mühlenbernd, H.; Li, G.; Bai, B.; Tan, Q.; Jin, G.; Zentgraf, T.; Zhang, S. Dispersionless Phase Discontinuities for Controlling Light Propagation. *Nano Lett.* **2012**, *12*, 5750–5755. [CrossRef]

24.　Zaman, M.A.; Padhy, P.; Hesselink, L. Solenoidal optical forces from a plasmonic Archimedean spiral. *Phys. Rev. A* **2019**, *100*, 013857. [CrossRef]

25.　Tsai, W.-Y.; Huang, J.-S.; Huang, C.-B. Selective Trapping or Rotation of Isotropic Dielectric Microparticles by Optical Near Field in a Plasmonic Archimedes Spiral. *Nano Lett.* **2014**, *14*, 547–552. [CrossRef]

26.　Zhang, Y.; Zhang, R.; Li, X.; Ma, L.; Liu, C.; He, C.; Cheng, C. Radially polarized plasmonic vector vortex generated by a metasurface spiral in gold film. *Opt. Express* **2017**, *25*, 32150–32160. [CrossRef] [PubMed]

27.　Kim, M.; Lee, D.; Yang, Y.; Kim, Y.; Rho, J. Reaching the highest efficiency of spin Hall effect of light in the near-infrared using all-dielectric metasurfaces. *Nat. Commun.* **2022**, *13*, 2036. [CrossRef]

28.　Luo, W.; Sun, S.; Xu, H.-X.; He, Q.; Zhou, L. Transmissive Ultrathin Pancharatnam-Berry Metasurfaces with nearly 100% Efficiency. *Phys. Rev. A* **2017**, *7*, 044033. [CrossRef]

29.　Yuan, Y.; Zhang, K.; Ratni, B.; Song, Q.; Ding, X.; Wu, Q.; Burokur, S.N.; Genevet, P. Independent phase modulation for quadruplex polarization channels enabled by chirality-assisted geometric-phase metasurfaces. *Nat. Commun.* **2020**, *11*, 4186. [CrossRef]

30.　Xiang, Z.; Shen, Z.; Shen, Y. Quasi-perfect vortices generated by Pancharatnam-Berry phase metasurfaces for optical spanners and OAM communication. *Sci. Rep.* **2022**, *12*, 1053. [CrossRef]

31.　Ni, J.; Huang, C.; Zhou, L.-M.; Gu, M.; Song, Q.; Kivshar, Y.; Qiu, C.-W. Multidimensional phase singularities in nanophotonics. *Science* **2021**, *374*, 418. [CrossRef] [PubMed]

32.　Forbes, A.; de Oliveira, M.; Dennis, M.R. Structured light. *Nat. Photonics* **2021**, *15*, 253–262. [CrossRef]

33.　Xie, X.; Chen, Y.; Yang, K.; Zhou, J. Harnessing the Point-Spread Function for High-Resolution Far-Field Optical Microscopy. *Phys. Rev. Lett.* **2014**, *113*, 263901. [CrossRef]

34.　Roxworthy, B.J.; Toussaint, K.C. Optical trapping with pi-phase cylindrical vector beams. *New J. Phys.* **2010**, *12*, 073012. [CrossRef]

35.　Yuanjie, Y.; Yuxuan, R.; Mingzhou, C.; Yoshihiko, A.; Carmelo, R.-G. Optical trapping with structured light: A review. *Adv. Photonics* **2021**, *3*, 034001. [CrossRef]

36.　He, C.; He, H.; Chang, J.; Chen, B.; Ma, H.; Booth, M.J. Polarisation optics for biomedical and clinical applications: A review. *Light Sci. Appl.* **2021**, *10*, 194. [CrossRef]

37.　Sit, A.; Bouchard, F.; Fickler, R.; Gagnon-Bischoff, J.; Larocque, H.; Heshami, K.; Elser, D.; Peuntinger, C.; Günthner, K.; Heim, B.; et al. High-dimensional intracity quantum cryptography with structured photons. *Optica* **2017**, *4*, 1006–1010. [CrossRef]

38.　Rosales-Guzmán, C.; Bhebhe, N.; Forbes, A. Simultaneous generation of multiple vector beams on a single SLM. *Opt. Express* **2017**, *25*, 25697–25706. [CrossRef]

39.　Parigi, V.; D'Ambrosio, V.; Arnold, C.; Marrucci, L.; Sciarrino, F.; Laurat, J. Storage and retrieval of vector beams of light in a multiple-degree-of-freedom quantum memory. *Nat. Commun.* **2015**, *6*, 7706. [CrossRef]

40.　Cardano, F.; Massa, F.; Qassim, H.; Karimi, E.; Slussarenko, S.; Paparo, D.; de Lisio, C.; Sciarrino, F.; Santamato, E.; Boyd, R.W.; et al. Quantum walks and wavepacket dynamics on a lattice with twisted photons. *Sci. Adv.* **2015**, *1*, e1500087. [CrossRef]

41.　Graham, T.M.; Bernstein, H.J.; Wei, T.-C.; Junge, M.; Kwiat, P.G. Superdense teleportation using hyperentangled photons. *Nat. Commun.* **2015**, *6*, 7185. [CrossRef] [PubMed]

42.　Ndagano, B.; Perez-Garcia, B.; Roux, F.S.; McLaren, M.; Rosales-Guzman, C.; Zhang, Y.; Mouane, O.; Hernandez-Aranda, R.I.; Konrad, T.; Forbes, A. Characterizing quantum channels with non-separable states of classical light. *Nat. Phys.* **2017**, *13*, 397–402. [CrossRef]

43.　Toninelli, E.; Ndagano, B.; Vallés, A.; Sephton, B.; Nape, I.; Ambrosio, A.; Capasso, F.; Padgett, M.J.; Forbes, A. Concepts in quantum state tomography and classical implementation with intense light: A tutorial. *Adv. Opt. Photonics* **2019**, *11*, 67–134. [CrossRef]

44.　Yan, H.; Li, S.; Xie, Z.; Zheng, X.; Zhang, H.; Zhou, B. Design of PANDA ring-core fiber with 10 polarization-maintaining modes. *Photonics Res.* **2017**, *5*, 1–5. [CrossRef]

45.　Vasilyeu, R.; Dudley, A.; Khilo, N.; Forbes, A. Generating superpositions of higher–order Bessel beams. *Opt. Express* **2009**, *17*, 23389–23395. [CrossRef] [PubMed]

46.　Naidoo, D.; Roux, F.S.; Dudley, A.; Litvin, I.; Piccirillo, B.; Marrucci, L.; Forbes, A. Controlled generation of higher-order Poincaré sphere beams from a laser. *Nat. Photonics* **2016**, *10*, 327–332. [CrossRef]

47.　Wan, H.; Wang, J.; Zhang, Z.; Cai, Y.; Sun, B.; Zhang, L. High efficiency mode-locked, cylindrical vector beam fiber laser based on a mode selective coupler. *Opt. Express* **2017**, *25*, 11444–11451. [CrossRef]

48.　Yan, H.; Zhang, E.; Zhao, B.; Duan, K. Free-space propagation of guided optical vortices excited in an annular core fiber. *Opt. Express* **2012**, *20*, 17904–17915. [CrossRef]

49. Li, S.; Wang, J. Multi-Orbital-Angular-Momentum Multi-Ring Fiber for High-Density Space-Division Multiplexing. *IEEE Photonics J.* **2013**, *5*, 7101007. [CrossRef]

50. García-García, J.; Rickenstorff-Parrao, C.; Ramos-García, R.; Arrizón, V.; Ostrovsky, A.S. Simple technique for generating the perfect optical vortex. *Opt. Lett.* **2014**, *39*, 5305–5308. [CrossRef]

51. Ostrovsky, A.S.; Rickenstorff-Parrao, C.; Arrizón, V. Generation of the "perfect" optical vortex using a liquid-crystal spatial light modulator. *Opt. Lett.* **2013**, *38*, 534–536. [CrossRef]

52. Vaity, P.; Rusch, L. Perfect vortex beam: Fourier transformation of a Bessel beam. *Opt. Lett.* **2015**, *40*, 597–600. [CrossRef]

53. Dong, M.; Yang, Z.; Chao, Z.; Hua, L.; Cong, W.; Han, Z.; Wending, Z.; Ting, M.; Jianlin, Z. Generation of polarization and phase singular beams in fibers and fiber lasers. *Adv. Photonics* **2021**, *3*, 014002. [CrossRef]

54. Li, P.; Zhang, Y.; Liu, S.; Ma, C.; Han, L.; Cheng, H.; Zhao, J. Generation of perfect vectorial vortex beams. *Opt. Lett.* **2016**, *41*, 2205–2208. [CrossRef]

55. Fu, S.; Gao, C.; Wang, T.; Zhang, S.; Zhai, Y. Simultaneous generation of multiple perfect polarization vortices with selective spatial states in various diffraction orders. *Opt. Lett.* **2016**, *41*, 5454–5457. [CrossRef] [PubMed]

56. Li, D.; Chang, C.; Nie, S.; Feng, S.; Ma, J.; Yuan, C. Generation of elliptic perfect optical vortex and elliptic perfect vector beam by modulating the dynamic and geometric phase. *Appl. Phys. Lett.* **2018**, *113*, 121101. [CrossRef]

57. Liu, Y.; Ke, Y.; Zhou, J.; Liu, Y.; Luo, H.; Wen, S.; Fan, D. Generation of perfect vortex and vector beams based on Pancharatnam-Berry phase elements. *Sci. Rep.* **2017**, *7*, 44096. [CrossRef]

58. Liu, Z.; Liu, Y.; Ke, Y.; Liu, Y.; Shu, W.; Luo, H.; Wen, S. Generation of arbitrary vector vortex beams on hybrid-order Poincaré sphere. *Photonics Res.* **2017**, *5*, 15–21. [CrossRef]

59. Bao, Y.; Ni, J.; Qiu, C.-W. A Minimalist Single-Layer Metasurface for Arbitrary and Full Control of Vector Vortex Beams. *Adv. Mater.* **2020**, *32*, 1905659. [CrossRef]

60. Wang, E.; Shi, L.; Niu, J.; Hua, Y.; Li, H.; Zhu, X.; Xie, C.; Ye, T. Multichannel Spatially Nonhomogeneous Focused Vector Vortex Beams for Quantum Experiments. *Adv. Opt. Mater.* **2019**, *7*, 1801415. [CrossRef]

61. Zhang, Y.-Q.; Zeng, X.-Y.; Zhang, R.-R.; Zhan, Z.-J.; Li, X.; Ma, L.; Liu, C.-X.; He, C.-W.; Cheng, C.-F. Generation of a plasmonic radially polarized vector beam with linearly polarized illumination. *Opt. Lett.* **2018**, *43*, 4208–4211. [CrossRef]

62. Yue, F.; Wen, D.; Xin, J.; Gerardot, B.D.; Li, J.; Chen, X. Vector Vortex Beam Generation with a Single Plasmonic Metasurface. *ACS Photonics* **2016**, *3*, 1558–1563. [CrossRef]

63. Liu, M.; Huo, P.; Zhu, W.; Zhang, C.; Zhang, S.; Song, M.; Zhang, S.; Zhou, Q.; Chen, L.; Lezec, H.J.; et al. Broadband generation of perfect Poincaré beams via dielectric spin-multiplexed metasurface. *Nat. Commun.* **2021**, *12*, 2230. [CrossRef] [PubMed]

64. Yang, Q.; Xie, Z.; Zhang, M.; Ouyang, X.; Xu, Y.; Cao, Y.; Wang, S.; Zhu, L.; Li, X. Ultra-secure optical encryption based on tightly focused perfect optical vortex beams. *Nanophotonics* **2022**, *11*, 1063–1070. [CrossRef]

65. Shao, W.; Huang, S.; Liu, X.; Chen, M. Free-space optical communication with perfect optical vortex beams multiplexing. *Opt. Commun.* **2018**, *427*, 545–550. [CrossRef]

66. Wang, W.; Wang, P.; Pang, W.; Pan, Y.; Nie, Y.; Guo, L. Evolution Properties and Spatial-Mode UWOC Performances of the Perfect Vortex Beam Subject to Oceanic Turbulence. *IEEE Trans. Commun.* **2021**, *69*, 7647–7658. [CrossRef]

67. Chen, M.; Mazilu, M.; Arita, Y.; Wright, E.M.; Dholakia, K. Dynamics of microparticles trapped in a perfect vortex beam. *Opt. Lett.* **2013**, *38*, 4919–4922. [CrossRef]

68. Han, L.; Liu, S.; Li, P.; Zhang, Y.; Cheng, H.; Zhao, J. Catalystlike effect of orbital angular momentum on the conversion of transverse to three-dimensional spin states within tightly focused radially polarized beams. *Phys. Rev. A* **2018**, *97*, 053802. [CrossRef]

69. Guo, X.; Li, P.; Zhong, J.; Liu, S.; Wei, B.; Zhu, W.; Qi, S.; Cheng, H.; Zhao, J. Tying Polarization-Switchable Optical Vortex Knots and Links via Holographic All-Dielectric Metasurfaces. *Laser Photonics Rev.* **2020**, *14*, 1900366. [CrossRef]

70. Zuo, R.; Liu, W.; Cheng, H.; Chen, S.; Tian, J. Breaking the Diffraction Limit with Radially Polarized Light Based on Dielectric Metalenses. *Adv. Opt. Mater.* **2018**, *6*, 1800795. [CrossRef]

71. Li, Y.; Cao, L.; Wen, Z.; Qin, C.; Yang, J.; Zhang, Z.; Liang, G.; Shang, Z.; Zhang, K.; Zhang, S.; et al. Broadband quarter-wave birefringent meta-mirrors for generating sub-diffraction vector fields. *Opt. Lett.* **2019**, *44*, 110–113. [CrossRef]

72. Lin, J.; Mueller, J.P.B.; Wang, Q.; Yuan, G.; Antoniou, N.; Yuan, X.-C.; Capasso, F. Polarization-Controlled Tunable Directional Coupling of Surface Plasmon Polaritons. *Science* **2013**, *340*, 331–334. [CrossRef] [PubMed]

73. Zhang, R.; Zhang, Y.; Ma, L.; Zeng, X.; Li, X.; Zhan, Z.; Ren, X.; He, C.; Liu, C.; Cheng, C. Nanoscale optical lattices of arbitrary orders manipulated by plasmonic metasurfaces combining geometrical and dynamic phases. *Nanoscale* **2019**, *11*, 14024–14031. [CrossRef]

74. Zeng, X.; Zhang, Y.; Gu, M.; Zhan, Z.; Zhang, R.; Zhang, Y.; Sun, R.; He, C.; Liu, C.; Cheng, C. Arbitrary manipulations of focused higher-order Poincaré beams by a Fresnel zone metasurface with alternate binary geometric and propagation phases. *Photonics Res.* **2022**, *10*, 1117–1126. [CrossRef]

75. Teperik, T.V.; Archambault, A.; Marquier, F.; Greffet, J.J. Huygens-Fresnel principle for surface plasmons. *Opt. Express* **2009**, *17*, 17483–17490. [CrossRef]

76. RefractiveIndex.INFO-Refractive Index Database. Available online: https://refractiveindex.info/ (accessed on 11 March 2023).

77. Babar, S.; Weaver, J.H. Optical constants of Cu, Ag, and Au revisited. *Appl. Opt.* **2015**, *54*, 477–481. [CrossRef]

78. Malitson, I.H. Interspecimen Comparison of the Refractive Index of Fused Silica*,†. *J. Opt. Soc. Am.* **1965**, *55*, 1205–1209. [CrossRef]

79. Zhan, Q. Cylindrical vector beams: From mathematical concepts to applications. *Adv. Opt. Photonics* **2009**, *1*, 1–57. [CrossRef]

80. Lu, T.H.; Huang, T.D.; Wang, J.G.; Wang, L.W.; Alfano, R.R. Generation of flower high-order Poincaré sphere laser beams from a spatial light modulator. *Sci. Rep.* **2016**, *6*, 39657. [CrossRef] [PubMed]

81. Milione, G.; Evans, S.; Nolan, D.A.; Alfano, R.R. Higher Order Pancharatnam-Berry Phase and the Angular Momentum of Light. *Phys. Rev. Lett.* **2012**, *108*, 190401. [CrossRef]